AIAA JOURNAL
Vol. 42, No. 12, December 2004

Ghost-Cell Method for Inviscid Two-Dimensional Flows on Cartesian Grids

A. Dadone*
Politecnico di Bari, 70125 Bari, Italy
and
B. Grossman†
Virginia Polytechnic Institute and State University, Blacksburg, Virginia 24061

A new approach to the computation of inviscid flows using Cartesian grid methods is presented. The crux of the method is the curvature-corrected symmetry technique (CCST) developed by the present authors for body-fitted grids and reviewed here. The method introduces ghost cells near the boundaries whose values are developed from an assumed flowfield model in the vicinity of the wall consisting of a vortex flow that satisfies the normal momentum equation and the nonpenetration condition. The CCST boundary condition was shown to be substantially more accurate than traditional boundary-condition approaches. This improved boundary condition is adapted to a Cartesian mesh formulation that we term the ghost body-cell method. In this method, all cell centers exterior to the body are computed with fluxes at the four surrounding cell edges. There is no need for special treatment corresponding to "cut cells," which complicate other Cartesian mesh methods. The merits of the method are indicated by the computation of the compressible flow about basic circular cylinders as well as of airfoil applications and detailed comparisons to body-fitted grid computations. We show that the surface nonpenetration condition is satisfied in the limit of vanishing cell size and that the method is second-order accurate in space. In addition, we prove that the results are independent of the position of the body with respect to the grid. The flexibility of the approach is illustrated with an application to the flow over a multiple-body configuration. Finally, it is mentioned that the ghost body-cell method on Cartesian grids developed here appears to be particularly well suited for design optimization problems.

Introduction

THE continuous growing power of computers encourages engineers to rely on computational fluid dynamics for the design and testing of new technological solutions. Numerical simulations allow the analysis of the phenomena without resorting to expensive prototypes and complex experimental measurements. On the other hand, although simple geometries discretized by regular grids are efficiently handled by codes and hardware, flows with complex geometries requiring body-fitted grids are still challenging problems for today's computers. The grid generation process, whether for composite block structured grids or unstructured grids, is often laborious and is not always as automated as desired. The conceptual design process often requires detailed body-fitted grids over wide classes of different geometric topologies. Grid generation for complex topologies often takes weeks or even months to develop and this becomes a major impediment to using computational fluid dynamics in design. Further complications may occur due to moving boundaries or problems that require continuing regeneration or deformation of grids.

One approach to develop a simplified alternative to complex grid generation involves the use of Cartesian grid methods. In these methods the body does not coincide with grid surfaces or grid volume edges. Instead, the body is immersed in the grid and the complication of generating a body-fitted grid is exchanged for complications associated with the implementation of the surface boundary conditions. Furthermore, because the body surfaces are not aligned with the grid it is nearly impossible to adequately resolve high-Reynolds-number boundary layers with Cartesian mesh methods. Nonetheless, there are many classes of flow problems that benefit from the efficiency of Cartesian mesh approaches.

Cartesian mesh methods have their origin in transonic potential flow computations.[1,2] Early Cartesian Euler computations were performed in Refs. 3–5. More recent computations[6–8] involved the use of grid adaptation and have produced very good results on some very complex configurations. Aftosmis and Berger[9] have also shown that Cartesian mesh computations may be characterized by a truncation error that is approximately one order of magnitude smaller than the truncation error of computations on triangular or quadrilateral body-fitted grids.

For completeness, we mention two other approaches that hold promise for avoiding grid generation difficulties. One is a Cartesian grid method that simulates viscous flows using vorticity confinement[10] and the other is an approach in which a body-force term is used to simulate moving boundaries.[11,12]

Cartesian grid finite difference schemes for computing fluid dynamic problems (e.g., Ref. 5) have proven to be quite efficient but require a complex topological discrimination of the cells located near the body profile. Cartesian grid finite volume methods (e.g., Ref. 13) are more straightforward in that they allow the use of composite elements (cut cells) determined by the intersection between the Cartesian grid and the body profile. On the other hand, these methodologies may suffer stability problems when such composite elements become very small.

The use of Cartesian grids without composite elements avoids this stability problem. On the other hand, it significantly increases the problem of enforcing the nonpenetration condition at solid walls immersed in the Cartesian grid. For inviscid flows, the simple nonpenetration condition can be easily enforced at solid walls if body-fitted grids are used, because the grids are aligned with the wall. For Cartesian grids, appropriate flow conditions must be enforced at the cell centers surrounding the body. The accuracy of the computed flow solution obviously depends on how accurately the flow

Presented as Paper 2002-1059 at the 40th Aerospace Sciences Meeting, Reno, NV, 15–17 January 2002; received 4 February 2003; revision received 9 February 2004; accepted for publication 28 February 2004.

*Professor, Dipartimento di Ingegneria Meccanica e Gestionale, Sezione Macchine ed Energetica. Senior Member AIAA.

†Professor, Department of Aerospace and Ocean Engineering; currently Vice President for Education and Outreach, National Institute of Aerospace, Hampton, VA 23666. Fellow AIAA.

conditions are enforced at these cell centers. As a consequence, an accurate model of the flow near the solid wall is required if accurate flow solutions are sought on Cartesian grids.

Recently, a model able to accurately represent inviscid flows near the solid walls has been introduced by the present authors.[14] It has been named the curvature-corrected symmetry technique (CCST) and has been developed for body-fitted grids. The method considers solid walls as boundaries immersed in the flowfield and enforces conditions at ghost cell centers located inside the body in a position close to the wall. The ghost cell values are developed from an assumed flowfield model in the vicinity of the wall consisting of a vortex flow, which satisfies the normal momentum equation and the nonpenetration condition. This flowfield model enforces symmetry conditions for entropy and total enthalpy along a surface normal to the body. Then the flow computations are performed using these ghost cell centers without taking into account the presence of the wall. Obviously, the fluid dynamic parameters are continuously updated at these ghost cell centers to enforce the wall impermeability condition at each stage of the computation.

The CCST boundary condition has been shown to be significantly more accurate for a variety of inviscid flows and has been shown to be at least one order of magnitude more accurate in inviscid two-dimensional flows[14] as well as in inviscid three-dimensional flows.[15] Other researchers have successfully implemented this boundary condition (e.g., Ref. 16) and have reported excellent results using the CCST in a preconditioned Euler code.

The aim of the present paper is to utilize the CCST to introduce an innovative and accurate numerical technique to enforce nonpenetration conditions at solid walls in Cartesian grid computations. We call this approach a ghost body-cell method (GBCM). The suggested method uses only rectangular cells without having to define cut cells in the vicinity of the solid boundary. In this paper, we first describe the governing equations and the classical boundary conditions to enforce the nonpenetration condition at solid walls for body-fitted grids. Then the improved boundary condition called the CCST is presented. Finally, the CCST is extended to model the flow near solid walls immersed in a Cartesian grid, that is, the GBCM. Details related to sharp corners and trailing edges are also described. The merits of the method are indicated by the computation of the compressible flow about basic circular cylinders as well as of airfoil applications and comparisons to body-fitted grid computations. The flexibility of the method is illustrated with an application to the flow over a multiple-body configuration.

Governing Equations

The vector form of the two-dimensional Euler equations in a Cartesian coordinate system can be written as

$$\boldsymbol{q}_t + \boldsymbol{f}_x + \boldsymbol{g}_y = 0 \tag{1}$$

where the vector of conserved variables is given by

$$\boldsymbol{q} = [\rho, \rho u, \rho v, \rho e_0]^T \tag{2}$$

and the inviscid flux vectors are

$$\boldsymbol{f} = [\rho u, p + \rho u^2, \rho uv, \rho u h_0]^T$$

$$\boldsymbol{g} = [\rho v, \rho uv, p + \rho v^2, \rho v h_0]^T \tag{3}$$

where p, ρ, u, v are the pressure, the density, and the two Cartesian components of the velocity vector, respectively, and e_0 and h_0 represent the total energy and the total enthalpy per unit mass, respectively.

In the work presented here, a quadrilateral, cell-centered finite volume method has been implemented with a flux-difference-splitting algorithm[17] as the flow solver. A MUSCL-type extrapolation, with a formal second-order accuracy in space, has been applied to extrapolate the physical variables onto the left- and right-hand sides of each cell edge. However, the methods developed in this paper are applicable to other flow solvers.

Wall Boundary Conditions

Classical Nonpenetration Condition

We consider a cell-centered finite volume representation of Eqs. (1) and focus our attention on a quadrilateral cell of the computational volume. The flux vector across a cell edge can be expressed as

$$\boldsymbol{F} = [\rho\tilde{v}, n_x p + \rho u\tilde{v}, n_y p + \rho v\tilde{v}, \rho h_0 \tilde{v}]^T \tag{4}$$

where n_x and n_y are the direction cosines normal to the cell edge and $\tilde{v}$ is the corresponding velocity component:

$$\tilde{v} = n_x u + n_y v \tag{5}$$

Assume that this cell face is located on a solid boundary so that $\tilde{v} = 0$. We see from Eq. (4) that the only quantity required to compute the flux vector at this cell edge is the pressure at the wall. For a cell-centered scheme, there are several conventional ways to evaluate this pressure. The most common approach is to extrapolate from the interior of the flowfield. A first-order pressure extrapolation is often used whereby the wall pressure is taken as the value associated with the nearest cell center. A second-order pressure extrapolation (P-II) is also sometimes used with the wall pressure linearly extrapolated from the two nearest cell centers:

$$p_w = \tfrac{3}{2} p_1 - \tfrac{1}{2} p_2 \tag{6}$$

where subscripts 1 and 2 refer to these cell centers (Fig. 1). In another approach, the pressure may be extrapolated to satisfy the normal momentum equation. Yet another boundary-condition procedure utilizes a characteristic boundary condition. A description and comparison of these techniques together with their application to a shock reflection problem are reported in Ref. 14.

CCST: A More Accurate Nonpenetration Condition

The CCST described in Ref. 14 utilizes "ghost points" and a vortex model in the vicinity of the body surface. The procedure consists of first locating two rows of cell centers closest to the body surface inside the flow domain (points 1 and 2 in Fig. 1). Then two extra rows of cells are inserted (image cells or ghost cells) outside the computational flowfield, which are created by reflecting the internal cells 1 and 2 symmetrically with respect to the body surface (points -1 and -2 in Fig. 1). The fluid dynamic variables at the ghost cell centers are utilized to implement the nonpenetration condition at the wall. The ghost cell values are developed from an assumed flowfield model in vicinity of the wall consisting of a vortex flow with locally symmetric distribution of entropy and total enthalpy along a surface normal. This flow model satisfies the normal momentum equation, the nonpenetration boundary condition, and enforces antisymmetric normal derivatives $\partial S/\partial n$ and $\partial h_0/\partial n$ along the surface normal to the body in the vicinity of the body. These entropy and total enthalpy distributions will produce zero normal derivatives when the flow is irrotational and will satisfy Crocco's relationship even

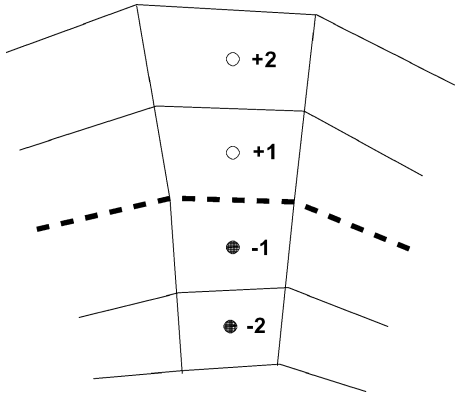

Fig. 1 Image cells for body-fitted grid implementation of CCST boundary condition.

when vorticity is present near the surface. The method has shown to produce superior accuracy[14] compared to the classical surface boundary condition procedures discussed in the previous subsection.

The pressure at the image cell centers is obtained from the integration of the normal momentum equation (for a steady inviscid flow):

$$p_{-i} = p_i - \rho_i\left(\tilde{u}_i^2 \big/ R_i\right)\Delta n_i \tag{7}$$

where the subscript i is equal to 1 or 2, Δn_i indicates the distance between the cell centers i and $-i$, and $\tilde{u}_i$ is the velocity component tangential to the body:

$$\tilde{u} = n_y u - n_x v \tag{8}$$

Note that R_i is the signed local radius of curvature of the wall, which is positive if the center of curvature is on the same side of the body and negative if the center of curvature is on the side of the flowfield.

The density and the velocity component tangential to the body are obtained from our vortex model:

$$\rho_{-i} = \rho_i (p_{-i}/p_i)^{1/\gamma}$$

$$\tilde{u}_{-i}^2 = \tilde{u}_i^2 + [2\gamma/(\gamma-1)](p_i/\rho_i - p_{-i}/\rho_{-i}) + \tilde{v}_i^2 - \tilde{v}_{-i}^2 \tag{9}$$

where the subscript i is equal to 1 or 2 and γ is the constant ratio of specific heats.

The velocity component normal to the body is obtained from the nonpenetration condition, following Ref. 14:

$$\tilde{v}_{-1} = -\tilde{v}_1$$

$$\tilde{v}_{-2} = 3\tilde{v}_{-1} + 2[\tilde{v}_1 + (\tilde{v}_1 - \tilde{v}_2)/2]\sqrt{\frac{\rho_1 + (\rho_1 - \rho_2)/2}{\rho_{-1} + (\rho_{-1} - \rho_{-2})/2}} \tag{10}$$

Numerical experiments have also shown that $\tilde{v}_{-2}$ can be approximated by a value antisymmetric to $\tilde{v}_2$. Then Eqs. (10) can be simplified as follows:

$$\tilde{v}_{-i} = -\tilde{v}_i \tag{11}$$

where the subscript i is equal to 1 or 2.

In Ref. 14 we show dramatic advantages of the CCST over conventional methods with regard to numerical entropy generation, total pressure loss, and grid convergence.

Ghost Body-Cell Method

In this section, the CCST will be extended to non-body fitted Cartesian grids. The method is developed for two-dimensional flows but may be extended to three dimensions. The numerical technique, GBCM, is described by the following steps:

1) The body is defined by a dense, ordered sequence of (x, y) coordinate pairs. The definition of the surface is completely independent of the mesh.

2) A Cartesian grid is selected and the computational flowfield is subdivided into finite volume cells.

3) The cell centers are discriminated between those located at the interior of the body and those located externally. The internal cell centers are flagged with $\lambda = 0$, while the external ones are flagged with $\lambda = 1$.

4) The row of cell centers closest to the body and located at the interior of the body is singled out. These cell centers are indicated by circles in Fig. 2, which presents a part of the cell center net and the curved body profile. (The right-hand side of the solid line is interior to the body.)

5) A second row of cell centers located at the interior of the body and adjacent to the first row is singled out. These cell centers are indicated by triangles in Fig. 2.

6) For each of the interior cell centers of the two rows described previously (ghost cell centers), a corresponding symmetric point is determined at a location exterior to the body and reflected symmetrically with respect to the body surface. To locate these symmetric points, we first determine the straight line passing through the cell center and orthogonal to the body. On this line, the point symmetric with the interior cell center with respect to the body is determined. These symmetric points are indicated by dark squares in Fig. 2. As an example, point B and interior cell center A in Fig. 2 are symmetric with respect to the body.

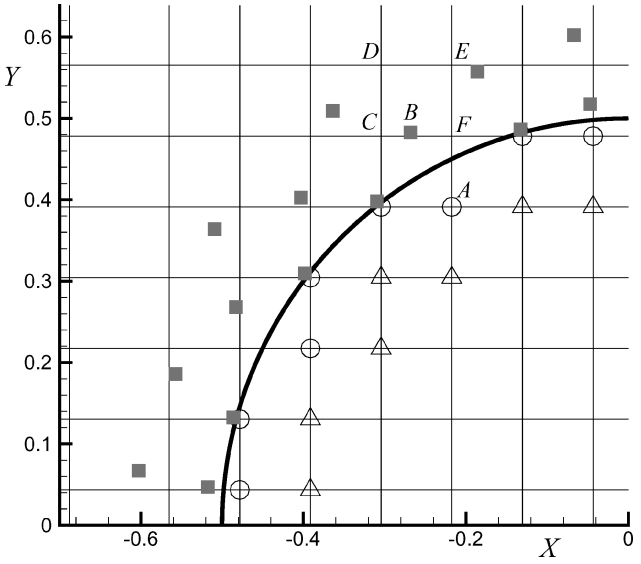

Fig. 2 Cartesian grid: cell center net, interior cell centers close to the body (open symbols), and symmetrically reflected exterior cell centers (solid symbols).

7) The four cell centers surrounding each symmetric point are determined. As an example, points C, D, E, and F are the cell centers surrounding point B in Fig. 2. Note that one or even two of these four cell centers may be located inside the body.

8) The value of the conserved variables $\boldsymbol{q}$ at the point B are determined by a bilinear interpolation:

$$\boldsymbol{q}_B = k_1(x - x_C)(y - y_C) + k_2(x - x_C) + k_3(y - y_C) + k_4 \tag{12}$$

where the constants $k_i (i = 1, \ldots, 4)$ are determined by the values of the conserved variables $\boldsymbol{q}$ at the cell centers C, D, E, and F. The bilinear interpolation is also used in situations when one or two of the cell centers surrounding point B are located inside the body surface. The internal values are determined from the CCST boundary condition (described next).

9) The values of the physical variables at the cell centers belonging to the previously defined two rows of internal cell centers are determined according to the CCST boundary condition, Eqs. (7), (9), and (11). As an example, the physical variables at cell center A are given by

$$p_A = p_B - \rho_B\left(\tilde{u}_B^2 \big/ R\right)\Delta n \tag{13}$$

$$\rho_A = \rho_B (p_A/p_B)^{1/\gamma} \tag{14}$$

$$\tilde{u}_A^2 = \tilde{u}_B^2 + [2\gamma/(\gamma-1)](p_B/\rho_B - p_A/\rho_A) \tag{15}$$

$$\tilde{v}_A = -\tilde{v}_B \tag{16}$$

In Eqs. (13–16), Δn is the distance between points A and B and R is the signed local radius of curvature of the body.

10) The time-dependent computation of all conserved variables at cell centers located external to the body now proceeds without any other boundary condition. Each cell center utilizes the fluxes at surrounding cell faces without further approximation. Cell centers located near the boundary utilize the interior (ghost) cells.

The time-dependent computation of the flowfield starts from the undisturbed flow condition enforced at all the cell centers located outside of the body, whereas stagnation flow conditions are enforced inside the body. In addition, the computed residuals are multiplied by

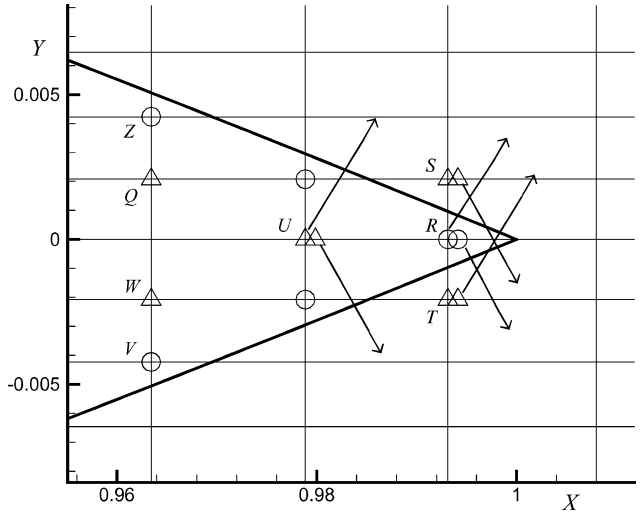

Fig. 3 Double-valued ghost cell centers near a sharp trailing edge.

λ. These assumptions are irrelevant to the flow computation and have been used to avoid any computational problem at the cell centers located inside the body. In addition, the last assumption enables a check of the variations of the residuals, which would never converge if the residual of the cell centers located inside the body are taken into account.

A special procedure based on double-valued cell centers is required near unresolved thin surfaces and sharp corners, such as at the sharp trailing edge of an airfoil. At sharp corners, one cell center inside the geometry may be the ghost cell center for one side of the corner surface as well as for the other side. Also, a ghost cell center pertaining to one side of the corner surface may be located in the flowfield on the other side of the sharp corner. One typical situation is shown in Fig. 3, where the first row of cell centers is again represented by circles and the second row by triangles. Note that point R has a symmetric point on the upper side of the trailing edge and a second symmetric point on the lower side. A similar situation holds for point U. In addition, point S belongs to the second row of ghost cell centers and has a symmetric point on the lower side of the trailing edge, while cell center T has a symmetric point located on the upper side. As a consequence, the cell centers R, S, T, and U will be double-valued. The procedure we use in this region is described by the following steps:

1) The sharp corner region is defined by detecting the body region where at least one of the ghost cell centers pertaining to one side of the sharp corner does not differ from the ghost cell centers pertaining to the other side or is located inside the flowfield. In Fig. 3, this region includes points R, S, T, and U. Note that cell centers V, W, Q, and Z do not belong to this region because the first two have symmetric points on the lower side and the other two cell centers have symmetric points on the upper side so that no cell center is double-valued.

2) The fluid dynamic properties at the ghost cell centers are computed by applying the previous procedure. Cell centers R and U, located inside the body, are characterized by two different sets of fluid dynamic properties evaluated by applying the previous procedure to both sides of the trailing edge. Also, cell centers S and T, located in the flowfield, are characterized by a first set of properties referring to the flowfield and by a second set computed by applying the previous procedure to the lower and upper sides of the trailing edge, respectively.

3) After computing the fluxes in a traditional manner, we recompute the fluxes involving the double values at cell centers R, S, T, and U.

4) We recompute the fluxes downstream of the trailing edge, involving the points R and U, by averaging the two sets of values at these points.

In GBCM, all cell centers exterior to the body are computed with fluxes at the four surrounding cell edges. There is no need for special treatment corresponding to cut cells, which complicate other Cartesian mesh methods. However, we do require special treatment for the evaluation of ghost cells. In our approach we also need surface normals and radii of curvature. Because our body is defined pointwise and is independent of the mesh, we may easily define the body with sufficient point density to allow straightforward accurate numerical calculation of the surface normals and radii of curvature. Numerical experiments have shown that, for the test cases used in this paper, the description of the body profile (in two dimensions) with 200 points, connected by segments, produces sufficiently accurate calculation of Δn and R.

Circular Cylinder Results

The subsonic compressible inviscid flow over a circular cylinder has been thoroughly analyzed to evaluate the merits of the GBCM for Cartesian grids. A freestream Mach number of $M_\infty = 0.38$ has been assumed. This flow condition produces a maximum Mach number of approximately 0.92 on the surface of the cylinder. The computations have been performed using three Cartesian grids: 110×110, 56×56, and 28×28. The numbers of cell centers located in the first row surrounding the body on the internal side were 128, 64, and 32, respectively. The far-field boundary was located at approximately 20 diameters.

First, three parameters have been used to evaluate the effectiveness of the new Cartesian grid technique. These include the L_2 norm of the normalized surface velocity component normal to the body, $\langle \tilde{v}_b \rangle$, the Mach number at the leading edge M_{le}, and the Mach number at the trailing edge M_{te}. These three parameters are plotted in Fig. 4 vs $1/N^2$, where N is the number of cell centers surrounding the body on the internal side. To generate the data for the curves in Fig. 4, the three parameters have been computed by interpolating the conserved variables at the body points from the four surrounding cell centers. Note that one or even two cell centers may be located inside the body. Figure 4 indicates that the GBCM enforces the nonpenetration condition in the limit of vanishing cell size and appears to be second-order accurate in space. We note that the errors in Fig. 4 are very small (of the order of 10^{-4}) when the finest grid is employed. Note that the freestream velocities are scaled to 1.

In addition, the flow has been also computed using three body-fitted polar grids, 128×32, 64×16, and 32×8, with the larger number corresponding to the number of cells located in the circumferential direction. The wall nonpenetration condition has been enforced by means of the classical P-II, as well as the CCST. We note that the number of cell centers surrounding the body on the internal side is the same for the three polar grids and the three corresponding

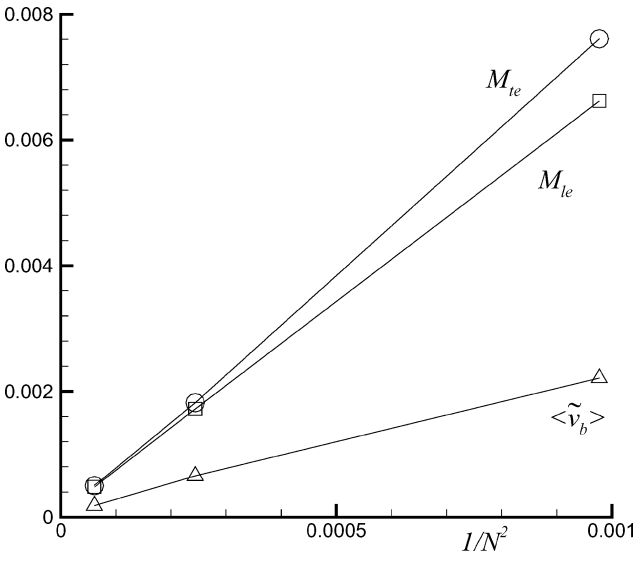

Fig. 4 Grid convergence of flow over circular cylinder using GBCMI: L_2 norm of the surface normal velocity component and Mach number at the leading and trailing edges.

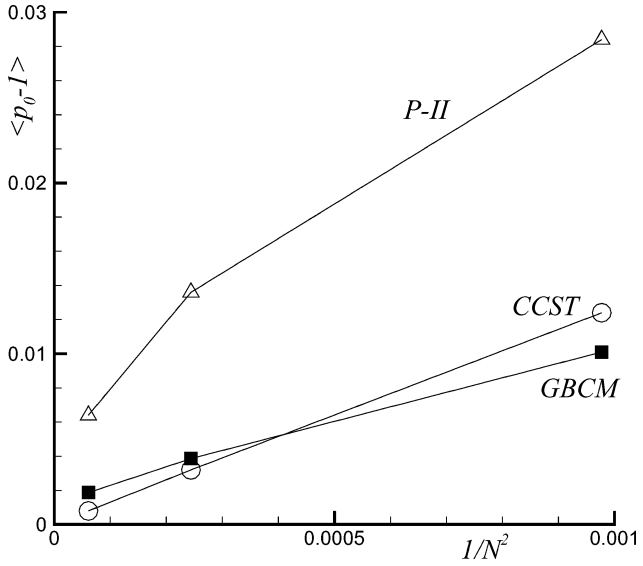

Fig. 5 Grid convergence for the flow over a circular cylinder: comparison between Cartesian mesh and body-fitted P-II and CCST results; L_2 norm of surface total pressure error.

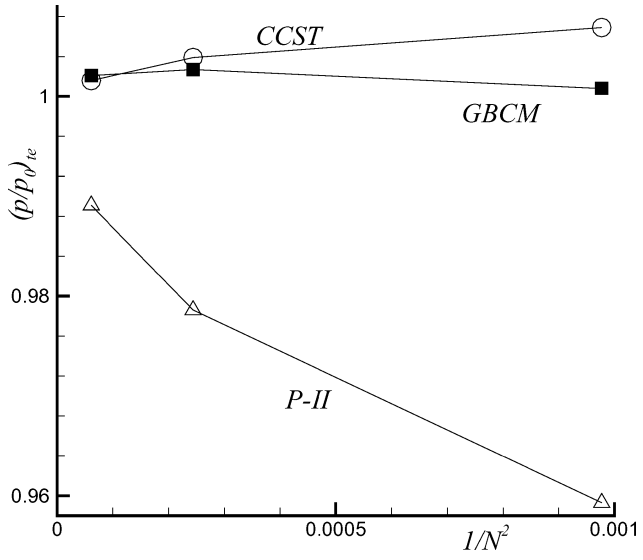

Fig. 6 Trailing-edge pressure grid convergence.

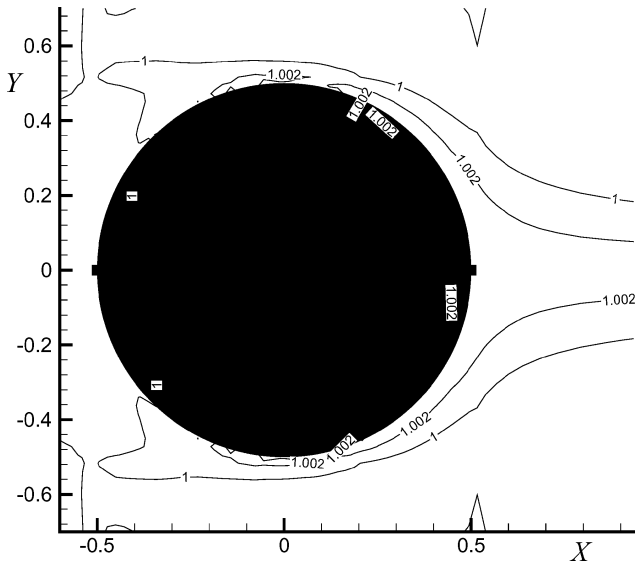

Fig. 7 Isobars of total pressure: GBCM on Cartesian grid.

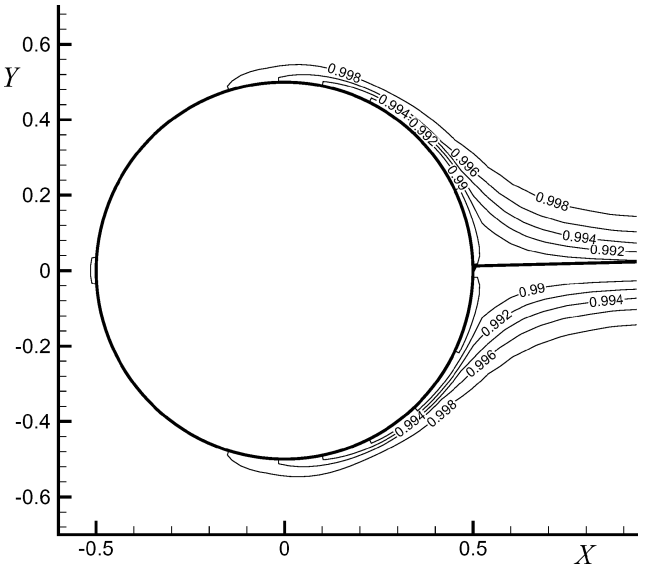

Fig. 8 Isobars of total pressure: P-II on body-fitted polar grid.

Cartesian grids. The results with the Cartesian grids (using GBCM) and with the body-fitted polar grids have been compared. The comparison is performed with respect to the number of cell centers used to discretize the body, that is, surrounding the body on the internal side. Figure 5 presents the L_2 norm of the normalized surface total pressure error, $\langle p_0 - 1 \rangle$, for the Cartesian grid GBCM, the body-fitted polar grid with P-II to the wall, and the body-fitted polar grid with CCST wall boundary conditions. The abscissa in Fig. 5 is again $1/N^2$. Similar results are plotted in Fig. 6, which shows the trailing-edge pressure divided by the freestream total pressure, $(p/p_0)_{\text{te}}$. From these results it appears that all of the methods are consistent and approach nearly the same value in the limit of vanishing cell size. However, GBCM results are remarkably converged in the grid and much more accurate than the classical P-II results on a body-fitted polar grid. Furthermore, they are as accurate as the CCST results on a body-fitted polar grid. In particular, notice the improved accuracy of the trailing-edge pressure, even at fine grids. We see that P-II has about a 1% error compared to the error in pressure at the trailing edge for CCST and GBCM which is approximately 0.1%.

Next, contour lines corresponding to the finest mesh results have been considered. The constant Mach number and the body-normal velocity contours produced by the Cartesian-grid GBCM and by the body-fitted CCST are almost symmetric and practically coincident, whereas the body-fitted polar grid P-II produces distorted patterns downstream of the cylinder with significant wake effects. These patterns are not reported here for the sake of conciseness and are presented in Ref. 18. Furthermore, Figs. 7 and 8 present the contours of the normalized total pressure. The contours found using the GBCM on Cartesian grids are very regular, with a very small total pressure increase, corresponding to a maximum error equal to 0.2%, which is quite close to the maximum error found with the CCST method on (body-fitted) polar grids.[18] In contrast, P-II yields significant total pressure errors, with a maximum equal to 1.4%.

Figures 5–8 indicate that the use of the GBCM for Cartesian grids preserves the superior accuracy of the CCST on body-fitted polar grids and shows dramatic advantages with respect to the widely used P-II on body-fitted polar grids.

Airfoil Results

Next we considered more general two-dimensional airfoil geometries. Airfoils are of course an important class of geometries, but they also serve as a test of the method for sharp corners, such as near sharp trailing edges. For these cases we apply the double-valued ghost-cell-center procedure for sharp corners outlined at the end of the section on the GBCM.

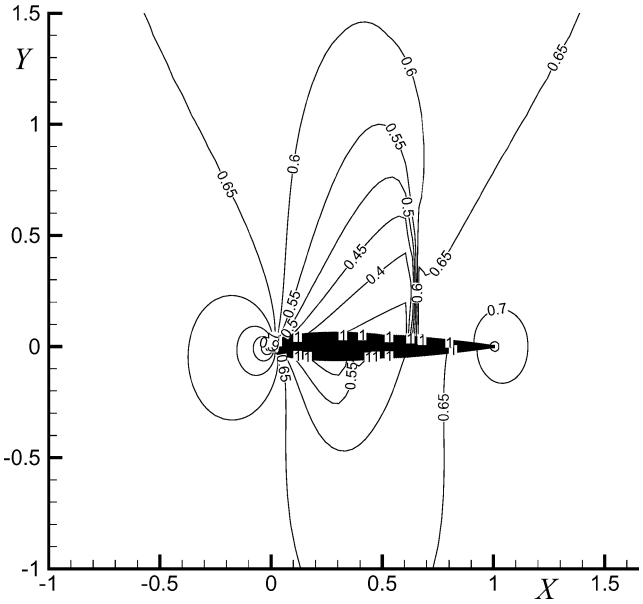

Fig. 9 Isobars for Cartesian grid calculation of flow over NACA0012 airfoil at M_∞ = 0.80, α = 1.25 deg.

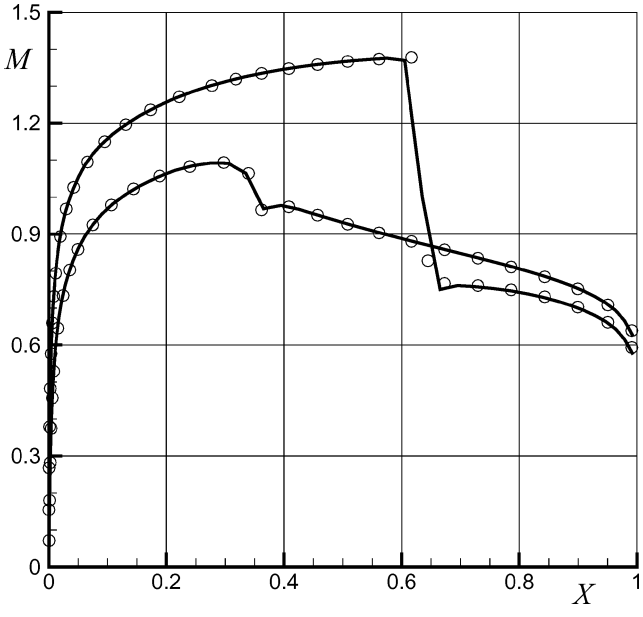

Fig. 10 Surface Mach-number distribution for NACA0012 airfoil at M_∞ = 0.80, α = 1.25 deg: ——, Cartesian grid and symbols, body-fitted CCST.

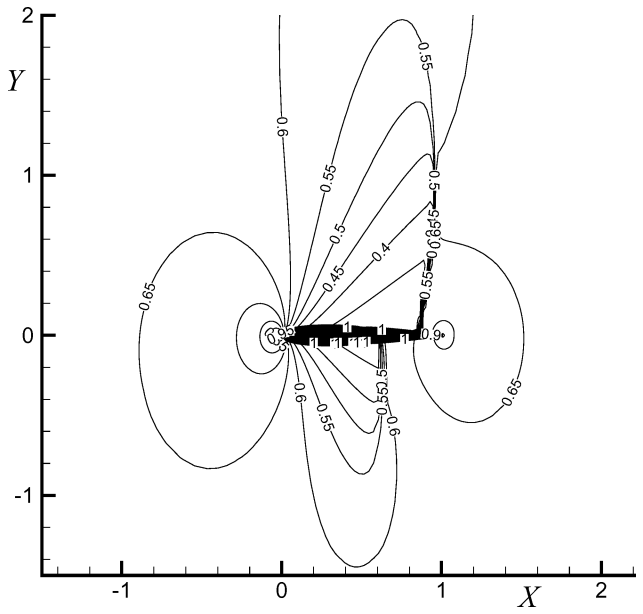

Fig. 11 Isobars for Cartesian grid calculation of flow over NACA0012 airfoil at M_∞ = 0.85, α = 1 deg.

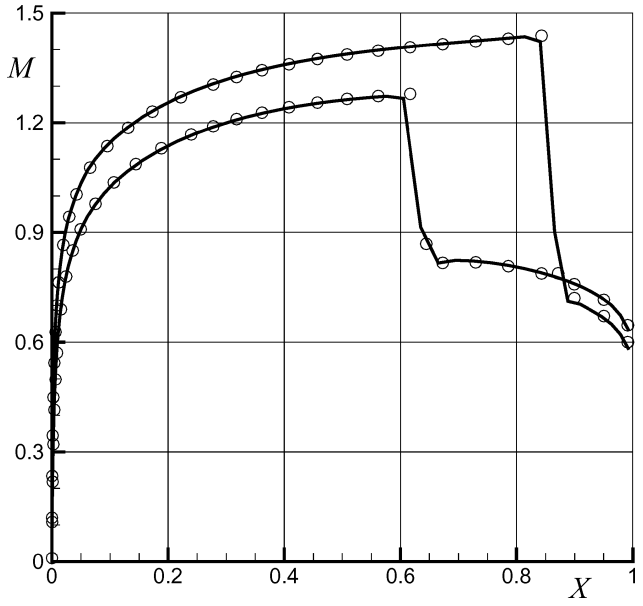

Fig. 12 Surface Mach-number distribution for NACA0012 airfoil at M_∞ = 0.85, α = 1 deg: ——, Cartesian grid and symbols, body-fitted CCST.

Results have been obtained for a NACA0012 airfoil. Various Mach numbers and angles of attack, corresponding to subsonic as well as transonic flow conditions, have been considered. Here we give some of these results. First we considered the subsonic flow corresponding to a freestream Mach number $M_\infty = 0.72$ at zero incidence. The computed isobars (reported in Ref. 18) indicate the symmetry of the computed solution while the computed Mach-number distribution[18] on the airfoil surface agrees quite well with the Mach-number distribution computed using an equivalent body-fitted grid and CCST. These results confirm the accuracy of the proposed method. In addition, the computed lift coefficient is of the order of 10^{-10}, further indicating the relevant symmetry of the computed solution. Another indication of the quality of the results is the computed drag coefficient of $C_D = 0.96 \times 10^{-4}$.

Then we considered the transonic flow corresponding to a freestream Mach number $M_\infty = 0.8$ at an angle of attack equal to 1.25 deg. Figure 9 presents the computed isobars (pressure divided by the freestream total pressure), whereas Fig. 10 shows the computed Mach-number distribution on the airfoil surface (continuous lines) compared with the body-fitted grid Mach-number distribution (symbols). The two sets of results in Fig.10 agree quite well. The computed lift and drag coefficients are: $C_L = 0.344$ and $C_D = 0.0220$. These values compare quite well with the results obtained by Salas and South (as discussed in Ref. 19, where their values $C_L = 0.3474$, and $C_D = 0.0221$ are described as accurate).

Finally, the sometimes difficult transonic flow test case, corresponding to $M_\infty = 0.85$ at an angle of attack equal to 1 deg, has been considered. The isobar pattern and Mach-number distribution are plotted in Figs. 11 and 12, respectively. The Cartesian grid and the body-fitted grid results compare very well. The computed lift and drag coefficients are $C_L = 0.372$ and $C_D = 0.0568$. They fall in the zone that is considered quite accurate in Ref. 20.

Then we investigated the influence of the leading-edge position with respect to the grid. The transonic test case with $M_\infty = 0.85$ at zero incidence has been considered. The flow was first computed

Table 1 Effects of the leading-edge position

Parameter	−50%	−25%	0%	+25%	+50%
p	2.78×10^{-4}	2.48×10^{-4}		4.12×10^{-4}	5.95×10^{-4}
ρ	2.41×10^{-4}	2.02×10^{-4}		3.14×10^{-4}	4.94×10^{-4}
Mach	4.95×10^{-4}	3.74×10^{-4}		5.07×10^{-4}	9.84×10^{-4}
u	4.63×10^{-4}	3.96×10^{-4}		4.44×10^{-4}	8.90×10^{-4}
v	3.82×10^{-4}	2.38×10^{-4}		3.63×10^{-4}	5.08×10^{-4}
$\langle T^\circ - 1 \rangle$	2.09×10^{-3}	2.07×10^{-3}	2.09×10^{-3}	2.04×10^{-3}	2.13×10^{-3}
$\langle \tilde{v} \rangle$	3.28×10^{-4}	3.68×10^{-4}	4.46×10^{-4}	3.98×10^{-4}	3.18×10^{-4}
C_L	$0\,(10^{-8})$	$0\,(10^{-11})$	$0\,(10^{-10})$	$0\,(10^{-7})$	$0\,(10^{-8})$
C_D	0.04612	0.04615	0.04616	0.04609	0.04607

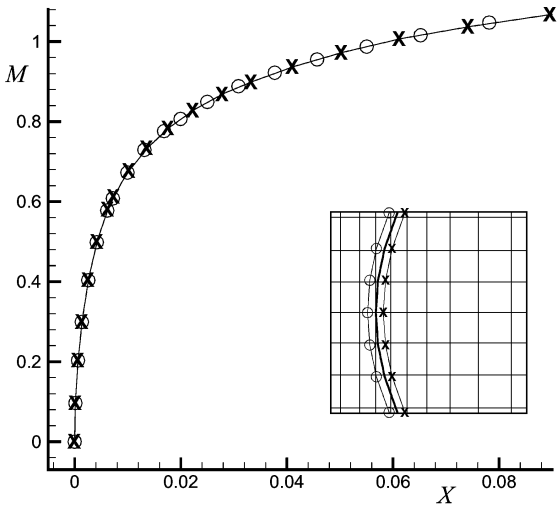

Fig. 13 Cartesian grid calculation of NACA0012 airfoil at $M_\infty = 0.85$, $\alpha = 0$ deg: surface Mach-number distribution in the leading-edge region (calculations performed with various leading-edge locations with respect to the grid as indicated by the inset).

by locating the leading edge precisely at a cell center, which will be considered the reference test case in the following. Then four more computations were been performed by moving the leading edge by −50, −25, 25, and 50% of the local cell dimension in the x direction. Figure 13 shows the Mach-number distribution in the leading-edge region for three of these computations: the continuous line corresponds to the leading-edge located coincident with the cell center, the circles indicate the results corresponding to the leading edge located 50% upstream, and finally the × symbols correspond to the leading-edge located 50% downstream. Note that the abscissa is measured from the leading-edge position. The position of the airfoil profile with respect to the cell center net is also shown in the small window in Fig. 13, using the same symbols already used for the Mach-number distribution. Note the position change of many cell centers when changing the location of the leading edge with respect to the cell center net: many cell centers located inside the body are moved to the flowfield and vice versa, so that the geometrical configuration presents large changes. Nevertheless, the three sets of Mach-number distributions coincide extremely well despite the effects of the curvature in this region and the changes in the geometrical configuration. This finding conclusively indicates that the method is practically independent of the airfoil profile location with respect to the grid.

To reinforce this conclusion, Table 1 presents the mean square difference between the surface values corresponding to the different grid locations for some fluid dynamic properties (pressure, density, Mach number, and the two velocity components). Also shown in Table 1 is the mean square error of the normalized total temperature on the body surface, $\langle T^\circ - 1 \rangle$, and of the normalized velocity component normal to the body surface, $\langle \tilde{v} \rangle$, together with the lift C_L and drag coefficients C_D for the five considered locations of the leading edge. Note that Table 1 contains interpolated values, which are used only for assessement purposes. Table 1 quantifies the effects of moving the leading edge with respect to the grid and establishes that the results are practically independent of the airfoil profile location with respect to the grid. This table also indicates that the normalized total temperature errors are very small (of the order of 10^{-3}) as well as the normalized velocity components normal to the body (of the order of 10^{-4}). This result is important to effectively utilize this method for application involving design optimization.

The final airfoil test cases that we performed were done to evaluate the curvature effects in Eq. (13), represented by the radius of curvature R. In particular, we investigated the effect of neglecting the curvature effect. We assumed this radius to be very large so that the pressure at points A and B in Fig. 2 becomes equal. This corresponds to changing the boundary conditions represented by Eqs. (13–16) into what we termed the symmetry conditions (SC) in Ref. 14 for the pressure, the density, and the velocity component tangential to the body, while an antisymmetric condition still holds for the velocity component normal to the body. With these (SC) we repeated the previous test case, that is, $M_\infty = 0.85$ at no incidence. The pressure coefficient distribution on the airfoil surface computed using GBCM agrees quite well with the results computed using the SC method (shown in Ref. 18), including the sensitive shock position and aftershock pressure coefficient distribution. However, the normal velocity component error at the body increases by a factor of five, while the total temperature error increases by 50%. This finding indicates that the curvature effects are important to obtain the highest levels of accuracy. Nevertheless, the results obtained by neglecting such effects are still very accurate. To have a more stringent test case for curvature effects we considered a subsonic case with $M_\infty = 0.40$ at an angle of attack of 6 deg. The corresponding pressure coefficient distribution on the airfoil surface is plotted in Fig. 14, where the continuous line indicates the GBCM results, while the symbols refer to the simplified SC results. We now observe that the SC results cannot capture the sharp pressure coefficient peak, whereas elsewhere the agreement between the two set of results is good. We also observed an increase in total temperature and normal velocity component errors quite similar to the previous test case increases. Furthermore, the lift coefficient was reduced by 2% using the simplified curvature treatment. This confirms that the SC method is less accurate than GBCM and, hence, it would require a finer grid to capture the sharpest details of the flowfield. Nevertheless, a good level of accuracy is still preserved. To prove once more the excellent quality of GBCM results, this last pressure distribution was also computed by employing the traditional CCST method on a body-fitted grid. The very good correspondence of the two sets of results, not reported here, again confirms the high level of accuracy of GBCM introduced here.

Bi-NACA Results

To show that the GBCM can be easily extended to multiple-body configurations, the external/internal flow over the so-called bi-NACA0012 double airfoil is considered here. The test case has been suggested for the Gesellschaft für Angewandte Mathematik und Mechanik workshop[20] on the numerical simulation of compressible

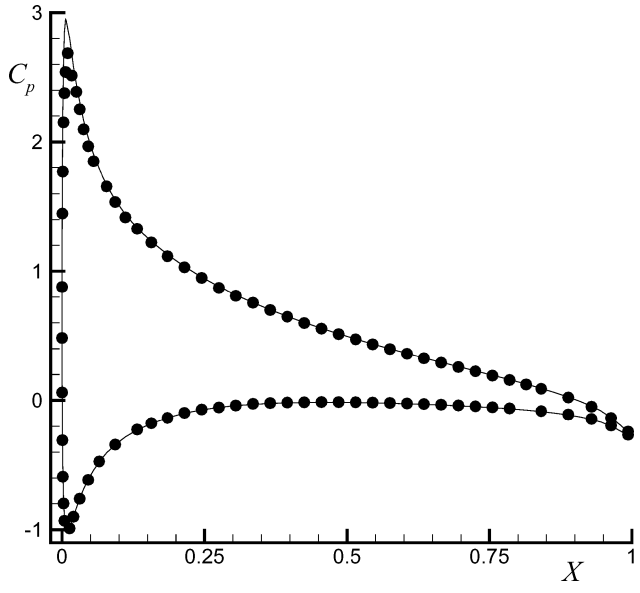

Fig. 14 Cartesian grid calculation of NACA0012 airfoil at $M_\infty = 0.40$, $\alpha = 6$ deg: surface pressure coefficient distribution compared for full GBCM (solid line) and neglecting curvature (symbols).

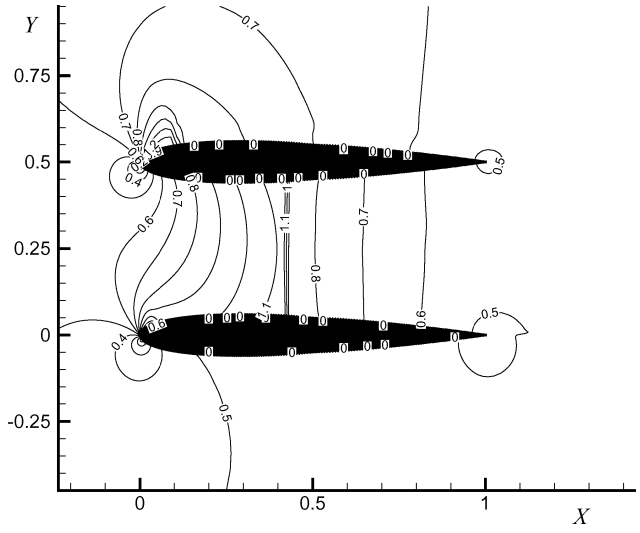

Fig. 15 Cartesian grid calculation of bi-NACA0012 double airfoil. Iso-Mach lines at $M_\infty = 0.55$, $\alpha = 6$ deg.

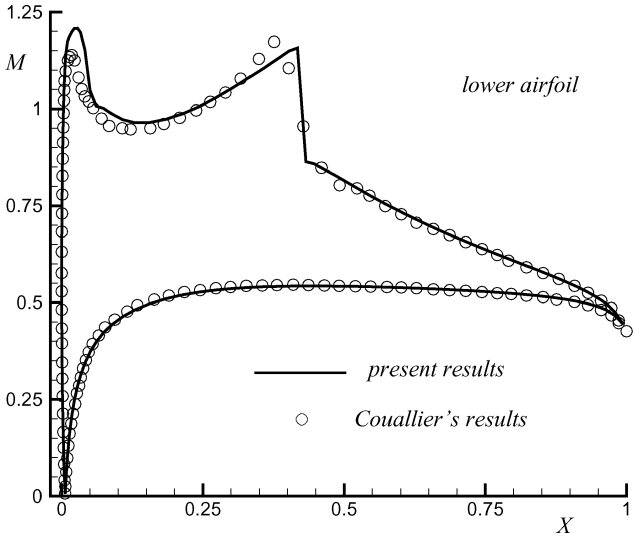

Fig. 16 Bi-NACA0012 double airfoil: surface Mach-number distribution on the lower airfoil at $M_\infty = 0.55$, $\alpha = 6$ deg.

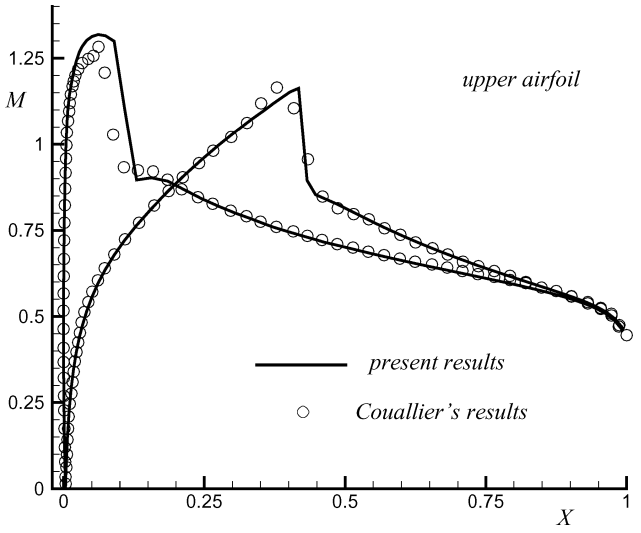

Fig. 17 Bi-NACA0012 double airfoil: surface Mach-number distribution on the upper airfoil at $M_\infty = 0.55$, $\alpha = 6$ deg.

Euler flows held at the Institut National de Recherche en Informatique et en Automatique in June 1986. The geometry of this test case, plotted in Fig. 15, is made up of two NACA0012 airfoils separated by a distance equal to 50% of the airfoil chord.

Three flow conditions were suggested in Ref. 20: a subsonic flow condition, a transonic flow with an internal shock, and a transonic flow with internal and external shocks. This last flow condition, which has the most interesting flow features, corresponds to an upstream Mach number $M_\infty = 0.55$ at an angle of attack of 6 deg. Five contributors considered this transonic test case and one author provided only the corresponding lift and drag coefficients.

The computation has been performed using a Cartesian grid with 140×202 cells with 104 cell centers located in the first row surrounding the body on the internal side. The corresponding iso-Mach lines are plotted in Fig. 15, and the surface Mach-number distributions on the lower and on the upper airfoils are shown as continuous lines in Figs. 16 and 17, respectively. Figures 15–17 indicate a multiple-shock situation.

On the upper side of both airfoils, there is a supersonic expansion due to the curvature of the leading edge, terminated by a sudden recompression: a shock on the upper airfoil and a supersonic recompression on the lower airfoil. This recompression is an important test because computational inaccuracies may degrade the supersonic recompression to a shock. Also, the internal region between the two airfoils is shaped as a nozzle where a supersonic expansion terminated by a shock takes place. In Ref. 20 the results by Couallier et al. were considered to be the most accurate of the five calculations presented. Those results were obtained using a computational domain subdivided into six subdomains using 177 nodes to describe the airfoil and are reproduced in Figs. 16 and 17 as symbols. The two sets of results show a reasonable overall agreement but with some differences: the shock locations are in good agreement, whereas differences can be observed upstream of the internal shock and in the leading-edge regions. The differences upstream of the internal shocks are due to a small overshoot exhibited by Couallier's results. This overshoot has a counterpart in Couallier's entropy results, which exhibit negative levels upstream of the internal shock. The leading-edge region differences require a deeper analysis, which shows that Couallier's results exhibit larger entropy errors in the leading-edge regions even though a finer mesh is used. These larger entropy errors reduce the expansion in these regions and determine the differences observed in Figs. 16 and 17. Indeed, GBCM coarse mesh results, mimicking Couallier's entropy errors, showed a better agreement with Couallier's results.

Conclusions

This paper presents a new approach to the computation of inviscid flows using Cartesian grid methods. The crux of the method is the CCST developed by the present authors for body-fitted grids. The method introduces ghost cells near the boundaries whose values are developed from an assumed flowfield model in the vicinity of the wall, consisting of a vortex flow with a symmetric distribution of entropy and total enthalpy along a local normal to the body surface. This model satisfies the normal momentum equation, the nonpenetration boundary condition, and Crocco's relation. The CCST boundary condition was shown to be substantially more accurate than traditional boundary-condition approaches. This improved boundary condition has been adapted to a Cartesian mesh formulation that we have termed the GBCM. In this method, all cell centers exterior to the body are computed with fluxes at the four surrounding cell edges. There is no need for special treatment corresponding to cut cells, which complicate other Cartesian mesh methods. The approach does require surface normals and radii of curvature. However, because our body is defined pointwise and is independent of the mesh, we may easily define the body with sufficient point density to allow straightforward accurate numerical calculation of the surface normals and radii of curvature.

A thorough investigation of the compressible inviscid flow about a circular cylinder has shown that the nonpenetration condition is satisfied in the limit of vanishing cell size, with errors in the velocity component normal to the body of the order of 10^{-4} for the finest grid employed (with freestream velocities scaled to 1). A mesh refinement study has indicated that the suggested method is second-order accurate in space.

The Cartesian grid results have then been compared with the results computed using the classical second-order pressure extrapolation P-II and the CCST on body-fitted polar grids. A mesh refinement study has been performed and the computed contours of Mach number and total pressure have been compared. These results have shown that the use of the GBCM on Cartesian grids preserves the superior accuracy of the CCST on body-fitted grids. In addition, the GBCM on Cartesian grids presents dramatic advantages with respect to the widely used P-II technique on body-fitted grids.

Results for subsonic and transonic flows about airfoils have shown that the GBCM can be easily extended to practical body shapes. The computed Mach-number distributions compare quite well with body-fitted grid results. The computed lift and drag coefficients match published values that are considered quite accurate. More important, the results have been conclusively shown to be independent of the position of the leading edge with respect to the grid. In addition, an analysis of the curvature effects shows that they improve the accuracy of the results. Nevertheless, sufficiently accurate results can be obtained also by simplifying the suggested model by dropping the curvature effects. The flexibility of the method has been finally illustrated with an application to the flow over a multiple-body configuration, the bi-NACA configuration. Comparison with published results has indicated the accuracy of the present results.

The method presented here may be extended to three-dimensional inviscid flows. Grid adaptation, particularly anisotropic adaptation, may also be applied for particularly complex geometries. It may be noted that because of the improved boundary treatment, the method without adaptation has been shown to produce accurate results for elementary two-dimensional geometries with relatively coarse grids. At present, any grid clustering near the body must be maintained to the far-field boundary. This is not a significant penalty in two-dimensional calculations, but it may become significant in three-dimensional calculations. Our future work will involve grid adaptation methods to address this issue. Finally, the GBCM on Cartesian grids appears to be particularly well suited for design optimization problems.

Acknowledgments

The research of the first author has been supported by the Italian Agency Ministero dell'Istruzione, dell'Università e della Ricerca. The first author is also grateful to M. J. Aftosmis of NASA Ames Research Center for a useful discussion on Cartesian grid methods.

References

[1]Boppe, C. W., "Transonic Flow Field Analysis for Wing-Fuselage Configurations," NASA CR-3243, May 1980.

[2]Wedan, B., and South, J. C., Jr., "A Method for Solving the Full-Potential Equation for General Configurations," AIAA Paper 83-1889, July 1983.

[3]Gaffney, R. L., Hassan, H. A., and Salas, M. D., "Euler Calculations for Wings Using Cartesian Grids," AIAA Paper 87-0356, Jan. 1987.

[4]Choi, S. K., and Grossman, B., "A Flux-Vector Split, Finite-Volume Method for Euler's Equations on Non-Mapped Grids," AIAA Paper 88-0227, Jan. 1988.

[5]Moretti, G., and Dadone, A., "Airfoil Calculations in Cartesian Grids," *Notes on Numerical Fluid Mechanics*, Vol. 24, 1989, pp. 423–434.

[6]De Zeeuw, D., and Powell, K. G., "An Adaptively Refined Cartesian Mesh Solver for the Euler Equations," *Journal of Computational Physics*, Vol. 104, 1993, pp. 56–68.

[7]Pember, R. B., Bell, J. B., Collela, P., Crutchfield, W. Y., and Welcome, M. L., "An Adaptive Cartesian Grid Method for Unsteady Compressible Flow in Irregular Regions," *Journal of Computational Physics*, Vol. 120, 1995, pp. 278–304.

[8]Melton, J. E., Berger, M. J., Aftosmis, M. J., and Wong, M. D., "3D Applications of a Cartesian Grid Euler Method," AIAA Paper 95-0853, Jan. 1995.

[9]Aftosmis, M. J., and Berger, M. J., "Multilevel Error Estimation and Adaptive h-Refinement for Cartesian Meshes with Embedded Boundaries," AIAA Paper 2002-0863, Jan. 2002.

[10]Wenren, Y., Steinhoff, J., Wang, L., and Fan, M., "Application of Vorticity Confinement to the Prediction of the Flow over Complex Bodies," AIAA Paper 2000-2621, Jan. 2000.

[11]Lai, M. C., and Peskin, C. S., "An Immersed Boundary Method with Formal Second Order Accuracy and Reduced Numerical Viscosity," *Journal of Computational Physics*, Vol. 160, 2000, pp. 705–721.

[12]Verzicco, R., Modh-Yusof, J., Orlandi, P., and Haworth, D., "Large Eddy Simulation in Complex Geometric Configurations Using Boundary Body Forces," *AIAA Journal*, Vol. 38, 2000, pp. 427–433.

[13]Aftosmis, M. J., *Solution Adaptive Cartesian Grid Methods for Aerodynamic Flows with Complex Geometries*, VKI Lecture Series 1997-02, von Kármán Inst. for Fluid Dynamics, Rhode Saint Genese, Belgium, 1997.

[14]Dadone, A., and Grossman, B., "Surface Boundary Conditions for the Numerical Solution of the Euler Equations," *AIAA Journal*, Vol. 32, 1994, pp. 285–293.

[15]Dadone, A., and Grossman, B., "Surface Boundary Conditions for the Numerical Solution of the Euler Equations in Three Dimensions," *Lecture Notes in Physics*, Vol. 453, 1995, pp. 188–194.

[16]Godfrey, A. G., Walters, R. W., and Van Leer, B., "Preconditioning for the Navier-Stokes Equations with Finite-Rate Chemistry," AIAA Paper 93-0535, Jan. 1993.

[17]Roe, P. L., "Characteristic Based Schemes for the Euler Equations," *Annual Review of Fluid Mechanics*, Vol. 18, 1986, pp. 337–365.

[18]Dadone, A., and Grossman, B., "An Immersed Body Methodology for Inviscid Flows on Cartesian Grids," AIAA Paper 2002-1059, Jan. 2002.

[19]Agard Fluid Dynamics Panel WG07, "Test Cases for Inviscid Flow Field Methods," AGARD-AR-211, 1985.

[20]Dervieux, A., Van Leer, B., Periaux, J., and Rizzi, A., (eds.), "Numerical Simulation of Compressible Euler Flows," *Notes on Numerical Fluid Mechanics*, Vol. 26, Vieweg, Brunswick, Germany, 1989.

K. Fujii
Associate Editor